Cell Reports
Physical Science

CellPress
OPEN ACCESS

Article

Glass-fiber-reinforced polymeric film as an efficient protecting layer for stable Li metal electrodes

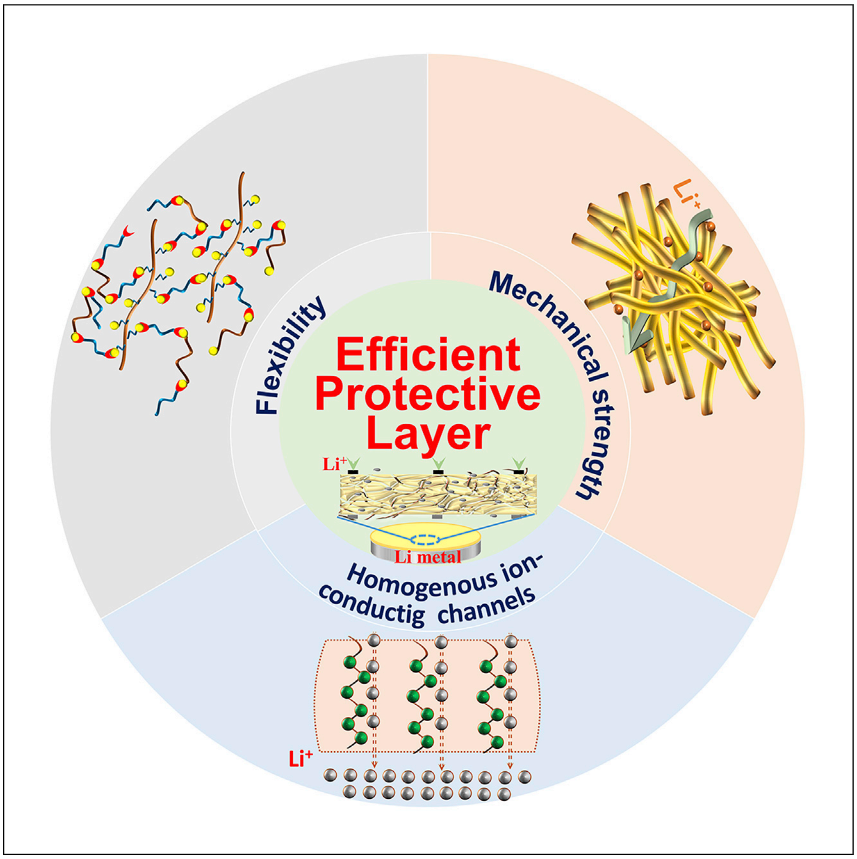

Gao et al. report a rationally designed multi-component hybrid protective film. Careful investigation of the role of each component in the hybrid protective film reveals the key attributes required to achieve an efficient protective layer for Li metal batteries with improved electrochemical performance.

Shilun Gao, Andrew Cannon, Feiyuan Sun, ..., Emily Ryan, Huabin Yang, Peng-Fei Cao

hb_yang@nankai.edu.cn (H.Y.)
caop@ornl.gov (P.-F.C.)

Highlights

Rationally designed hybrid protective films achieve ultra-stable Li metal electrode

Investigation of the individual role of each component in designed protective films

The key attributes of efficient protecting layers are unraveled.

Gao et al., Cell Reports Physical Science *2*, 100534
August 18, 2021 © 2021 The Authors.
https://doi.org/10.1016/j.xcrp.2021.100534

Cell Reports
Physical Science

CellPress
OPEN ACCESS

Article

Glass-fiber-reinforced polymeric film as an efficient protecting layer for stable Li metal electrodes

Shilun Gao,[1] Andrew Cannon,[2] Feiyuan Sun,[1] Yiyang Pan,[1] Dandan Yang,[3] Sirui Ge,[4] Nian Liu,[5] Alexei P. Sokolov,[6,7] Emily Ryan,[2] Huabin Yang,[1,8,*] and Peng-Fei Cao[6,9,*]

SUMMARY

With numerous reports on protecting films for stable lithium (Li) metal electrodes, the key attributes for how to construct these efficient layers have rarely been fully investigated. Here, we report a rationally designed hybrid protective layer (HPL) with each component aligning with one key attribute; i.e., cross-linked poly(dimethylsiloxane) (PDMS) enhances flexibility, polyethylene glycol (PEG) provides homogeneous ion-conducting channels, and glass fiber (GF) affords mechanical robustness. A significant improvement of the electrochemical performance of HPL-modified electrodes can be achieved in Li/HPL@Cu half cells, HPL@Li/HPL@Li symmetric cells, and HPL@Li/$LiFePO_4$ full cells. Even with an industrial standard $LiFePO_4$ cathode (96.8 wt % active material), the assembled cell still exhibits a capacity retention of 90% after 100 cycles at 1 C. More importantly, the functionality of each component has been studied comprehensively via electrochemical and physical experiments and simulations, which will provide useful guidance on how to construct efficient protective layers for next-generation energy storage devices.

INTRODUCTION

With the ever-increasing demand for portable electronics, electric vehicles, and grid-scale storage, developing next-generation rechargeable batteries with higher energy density is urgent and critical.[1–3] Lithium (Li) metal has been considered the ultimate anode material because of its ultrahigh theoretical specific capacity (3,860 mAh g^{-1}) and lowest negative electrochemical potential (−3.04 V versus the standard hydrogen electrode).[4–6] However, since the 1970s, when Li first served as the anode material in rechargeable batteries, Li metal batteries (LMBs) have been considered "unsafe" energy storage devices.[7,8] There are two main challenges that hinder commercialization of LMBs.[9,10] The first is dendritic Li growth. Because of non-uniform Li ion (Li^+) deposition during the cycling process, Li dendrites can penetrate the separator, cause a short circuit, and even cause thermal runaway of the battery.[11–13] In the subsequent cycling process, the Li dendrites may even be isolated from the bulk Li anode to form "dead" Li, resulting in rapid capacity fading.[14] The second is the structurally unstable intrinsic solid electrolyte interphase (SEI) layer. This layer inevitably gives rise to a non-uniform interfacial Li^+ flux and uncontrolled reactions between Li metal and electrolyte, leading to increased interfacial resistance and lower Coulombic efficiency (CE).[15–17] In the past decades, considerable efforts have been carried out to stabilize the SEI layer, improving the electrochemical performance of LMBs, including electrolyte modification,[18–20] separator

[1]Institute of New Energy Material Chemistry, School of Materials Science and Engineering, Nankai University, Tianjin 300350, China

[2]Department of Mechanical Engineering, Boston University, Boston, MA 02215, USA

[3]Experimental Teaching Center of Materials Science, School of Materials Science and Engineering, Nankai University, Tianjin 300350, China

[4]Department of Materials Science and Engineering, University of Tennessee, Knoxville, TN 37996, USA

[5]School of Chemical and Biomolecular Engineering, Georgia Institute of Technology, Atlanta, GA 30332, USA

[6]Chemical Sciences Division, Oak Ridge National Laboratory, Oak Ridge, TN 37830, USA

[7]Department of Chemistry, University of Tennessee, Knoxville, TN 37996, USA

[8]Tianjin Key Laboratory of Metal and Molecular Based Material Chemistry, School of Materials Science and Engineering, Nankai University, Tianjin 300350, China

[9]Lead contact

*Correspondence:
hb_yang@nankai.edu.cn (H.Y.),
caop@ornl.gov (P.-F.C.)

https://doi.org/10.1016/j.xcrp.2021.100534

modification,[21,22] designing micro/nanostructured three dimensional Li hosts,[23–25] and fabricating protective layers on the Li metal surface.[26] Among all of these strategies, constructing a protective layer on the Li metal surface is an emerging and effective approach to address these issues.[27–29]

With high flexibility and easy processability, tremendous research efforts have been devoted to polymeric protective films.[30–34] By regulating the Li^+ plating/stripping behavior, the protective layer on the Li metal surface can suppress the growth of dendritic Li and side reactions between the Li metal and electrolyte, contributing to enhanced electrochemical performance.[35] In this process, reasonable ionic conductivity of the polymer materials is highly required, and various polymers with non-polar groups (-[-OCH_2CH_2-]-),[32] polar groups (–CF, -NH, -COOH, -C = O -C≡N, etc.),[36,37] charged groups (Li^+ as counter ion),[38] and multi-type ionic conductive groups,[39,40] have been investigated for this purpose. However, as-prepared polymeric protective layers are usually mechanically weak and cannot efficiently suppress Li dendrite growth, especially under high current density and long-term cycling processes.[41,42] Polymer/inorganic filler hybrid protective layers have been regarded as a more desirable choice to enhance the interfacial stability of the Li metal anode.[43] By restricting the mobility of polymer chains, the inorganic fillers in the hybrid film can enhance the mechanical strength against severe interface fluctuation and dendrite growth upon cell cycling, contributing to enhanced electrochemical performance. For example, Jiang et al.[44] found that a Nafion film with only 1 wt % of TiO_2 displayed enhanced mechanical strength (~2 times) and improved cycling stability (a discharge capacity of 300 mAh g^{-1} higher than those with bare Li anodes after 100 cycles for Li/S cells). Xu et al.[45] prepared a polyvinylidene-*co*-hexafluoropropylene)/Li fluoride (PVDF-HFP/LiF) hybrid film with a Young's modulus of ~6.7 GPa versus 0.8 GPa for a pristine PVDF-HFP film, and in assembled Li/$LiFePO_4$ (Li/LFP) cells, a capacity retention of 80% can be maintained for a hybrid-layer-protected Li electrode after 250 cycles versus the same capacity retention after only 100 cycles for bare Li as the anode. Other hybrid protective films, like poly(3,4-ethylenedioxythiophene)-co-poly(ethylene glycol)/aluminum fluoride[46] and graphene/polydopamine,[47] with improved electrochemical performance compared with those with bare Li as the anode have also been reported. Although numerous studies have achieved stable Li electrodes by using polymeric or hybrid materials as protective layers, the key parameters of these high-performance protective layers have rarely been fully investigated, and such an achievement is especially meaningful for designing protecting films for practical applications of Li metal electrodes.

Here, we report a multi-component hybrid protective layer (HPL) with enhanced flexibility, abundant homogeneous ion-conducting channels, and outstanding mechanical robustness via rational component and structure design. With the combination of these improved attributes, cells with HPL-modified electrodes exhibit significantly enhanced electrochemical performance in symmetric cells (HPL@Li/HPL@Li), half cells (Li/HPL@Cu), and full cells (HPL@Li/LFP) even with an industrial standard LFP cathode (HPL@Li/C-LFP, 96.8 wt % active material). The advantage of the current design is that each component aligns with one key attribute: cross-linked poly(dimethylsiloxane) (PDMS) improves flexibility, polyethylene glycol (PEG) provides homogeneous ion-conducting channels, and glass fiber (GF) enhances mechanical strength. This allows us to evaluate the importance of each attribute by comprehensively studying the separate functionality of each component. Detailed experiments were carried out to understand the effects of their properties and were supplemented with computational simulations of the electrode-protective layer interface to better understand the physics of the system. The deep insights into the key

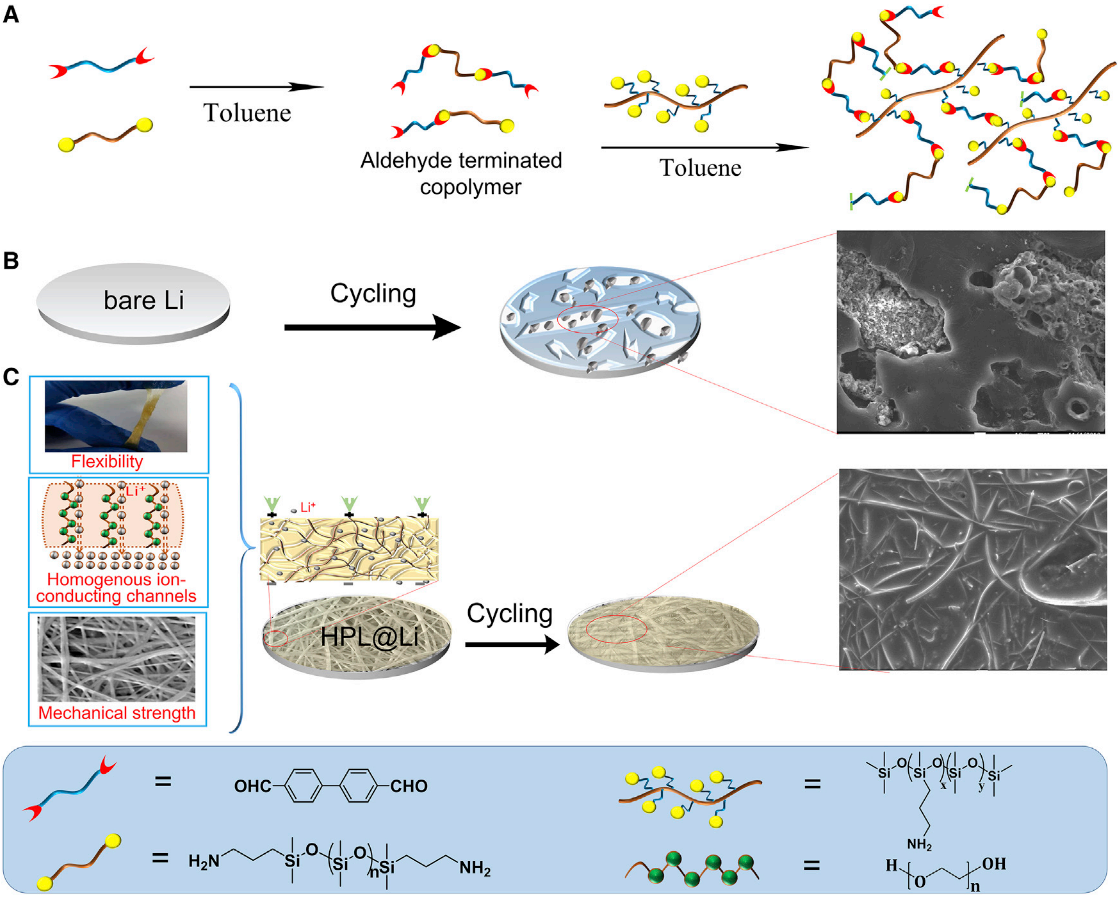

Scheme 1. Polymer fabrication process and schematic of different Li electrodes

(A) Schematic of the cross-linked PDMS fabrication process.

(B) Schematic of bare Li electrodes before and after the long-term cycling process and top-view images of bare Li after 50 cycles.

(C) Schematic of HPL components, the corresponding key attributes, and HPL-Li electrodes before and after the long-term cycling process; magnified images show the HPL after 50 cycles.

parameters of protective films gained during the current study will provide useful guidance to enable efficient protective layers on Li metal electrodes and advance development of high-performance LMBs with a prolonged cycle life.

RESULTS AND DISCUSSION

Preparation of the HPL

The viscoelasticity and dynamic behavior of the protective materials have been identified as playing an important role in regulating the Li^+ deposition on Li metal electrodes.[48,49] With intrinsic extensibility, good thermal/chemical stability, and fast segmental dynamics at ambient temperature, PDMS was selected as the flexible matrix to buffer the volume variation of the Li metal electrode during the cycling process.[50,51] As shown in Figure S1, the cross-linked PDMS (picture in Scheme 1A and Figure S2) was fabricated by forming imine bridges between the aminopropyl-terminated PDMS (PDMS-NH_2) with excess 4,4′-biphenyldicarboxaldehyde (BCA), followed by a cross-linking reaction using multi-amine functionalized PDMS (~48 amine groups per molecule).[52] In the infrared (IR) spectrum (Figure S3) of cross-linked PDMS, the appearance of a peak lying at 1,645 cm^{-1} suggests formation of an imine bond from the amine (780 cm^{-1}) and aromatic aldehyde (810 cm^{-1}) groups. It worth noting that the residue –NH_2 can also be detected from the IR spectrum.

According to previous reports of an amine-containing polymer for construction of 3D composite electrodes, separator modification, and functional additive in gel electrolyte, the presence of $-NH_2$ groups in the protective layers should also help with effective redistribution of Li^+ flux and a relatively homogeneous Li^+ deposition on the metal surface via affinity of its polar groups with Li^+ and Li metal.[53–55] Thermogravimetric analysis (TGA; Figure S4) demonstrates good thermal stability of cross-linked PDMS with no significant mass loss until 350°C. The frequency dependence of the oscillatory shear moduli for storage moduli (G′) and loss moduli (G′′) of the PDMS is displayed in Figure S5. The viscoelasticity of the polymer can be divided into the elastic component, depicted by G′, and the viscous component, described by G′′. The segmental relaxation time τ was estimated using the following equation:

$$\tau = \frac{1}{\omega_c},$$

where ω_c is determined from the crossover angular frequency.[56] The result shows that the storage modulus reaches 1 GPa, which is larger than the loss modulus ($G' > G''$) at $\sim 10^{11}$ rad s^{-1}, corresponding to a short relaxation time and fast segmental relaxation. The relatively low glass transition temperature (T_g) of cross-linked PDMS revealed by differential scanning calorimetry (DSC) ($T_g \sim -121°C$; Figure S6) also confirms its fast segmental relaxation at ambient temperature, which may play an important role in adapting to volumetric variation and remaining in conformal contact with the Li metal electrode even under high current density.

For bare Li electrode, the instrinsic SEI layer is mechanically unstable and cannot accommodate the huge volume variation of Li electrode during the repeated Li plating/stripping process as shwon in Scheme 1B. Considering the single PDMS component that cannot provide homogeneous ion-conducting channels, PEG (20 wt %) was added to the PDMS solution when preparing HPL.[57] With a porous structure and mechanical robustness, GF was selected to improve mechanical strength, and the high transparency of the GF after immersion in ethylene carbonate/diethyl carbonate (1:1 by volume) (Figures S7A and S7B) indicates its excellent wettability in the electrolyte solution. To construct the HPL for electrochemical studies (Scheme 1C, HPL components and structures), a quarter of the commercially available GF was taken out to form a composite with the homogeneous solution of PDMS and PEG on the Cu foil or Li metal surface. To evaluate the electrochemical performance of the cell with HPL-modified Cu foil or Li metal as electrode, Li/HPL@Cu half cells and HPL@Li/HPL@Li symmetric cells were initially assembled with an ether-based electrolyte (1 M Li bis(trifluoromethanesulfonyl)imide in 1,3-dioxolane//dimethyl ether, v/v = 1:1 and 2 wt % $LiNO_3$ as an additive), as shown in Figure 1A.

Electrochemical study of electrodes in half/symmetric cell configurations

It is known that in Li/Cu cells, a higher CE and longer lifespan indicate a high utilization ratio of Li metal electrode and stable Li^+ stripping/plating processes.[58,59] As shown in Figure 1B, at a current density of 1 mA cm^{-2}, the Li/HPL@Cu cell exhibits a superior cycling stability with an average CE of 96.5% after 300 cycles, which is in dramatic contrast to the Li/Cu cell (cell with bare Cu as electrode); i.e., rapid fading after 150 cycles. At a higher current density of 2 mA cm^{-2} (Figure 1C), an average CE of 94.8% can be achieved after 200 cycles for the Li/HPL@Cu cell versus a quick decay of CE with 18.4% after 168 cycles for the Li/Cu cell. Even at a current density of 3 mA cm^{-2}, a stable cycling performance can still be obtained for the Li/HPL@Cu cell with an average CE of 95.1% over 200 cycles (Figure 1D). To investigate the effect of the protective layer on the Cu foil, scanning electron microscopy (SEM) was used to examine the comparative surface morphologies of HPL@Cu and bare Cu

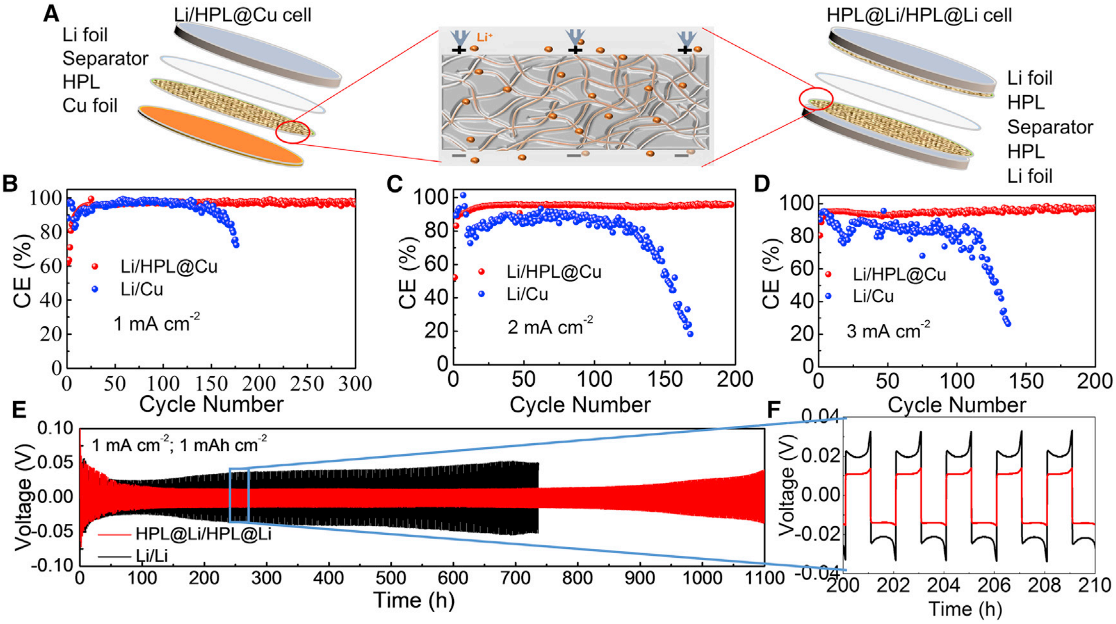

Figure 1. Electrochemical performance of Li/HPL@Cu and HPL@Li/HPL@Li cells

(A) Schematic of Li/HPL@Cu (left) and HPL@Li/HPL@Li (right) cells and the structure of the HPL.

(B–D) CEs of half cells with HPL@Cu or bare Cu as electrodes at a current density of 1 mA cm^{-2} with a capacity of 1 mAh cm^{-2}. The current density in (C) and (D) is 2 and 3 mA cm^{-2}, respectively.

(E) Cycling performance of symmetric cells with HPL@Li or bare Li as electrodes at a current density of 1 mA cm^{-2} with a capacity of 1 mAh cm^{-2}.

(F) Voltage profiles of selected cycles in (E).

foils after 10 cycles of the plating/stripping process (in the final state, the Cu foil was plated with Li and then disassembled for SEM testing), as shown in Figure S8. For the HPL@Cu electrode (Figures S8A and S8C), the HPL can efficiently prevent accumulation of Li^+ around "hotspots," enabling relatively homogeneous current distribution and facilitating uniform deposition of Li^+. In contrast, the bare Cu electrode exhibits a fractured and porous structured Li surface because of accumulation of "dead" Li (Figures S8B and S8D). Moreover, the charge-discharge profiles at different current densities also clearly confirm the significantly improved electrochemical performance of the Li/HPL@Cu cell. As shown in Figure S9, with increased current densities, an obviously decreased capacity can be observed for the Li/Cu cell, with a retention capacity of only ~0.2 mAh cm^{-2} after 150 cycles at 3 mA cm^{-2} versus a relatively high retention capacity of 0.9 mAh cm^{-2} for Li/HPL@Cu under the same condition.

Li/Li symmetric cell testing is utilized to monitor the Li plating/stripping behavior of Li metal electrodes, and lower voltage hysteresis indicates effective suppression of dendritic Li growth by the protective layer.[60] Figure S10A shown the potential profiles of HPL@Li/HPL@Li and Li/Li symmetric cells at a current density of 0.5 mA cm^{-2} with a fixed capacity of 0.5 mAh cm^{-2}. The Li/Li cell exhibits a fluctuating overpotential, which can probably be explained by accumulation of "dead" Li leading to increased ionic resistance. The HPL@Li/HPL@Li cell shows a much longer cycling life time of more than 1,350 h and maintains a stable overpotential of ~12–16 mV (versus Li^+/Li) after cycling for 100 h (Figures S10B and S10C), suggesting that the electrode reaches a steady state after the "activation" process. Under a higher current density (1 mA cm^{-2}, a capacity of 1 mAh cm^{-2}, as shown in Figures 1E and 1F), the Li/Li cell cycled with a gradually increasing overpotential over 600 h versus the

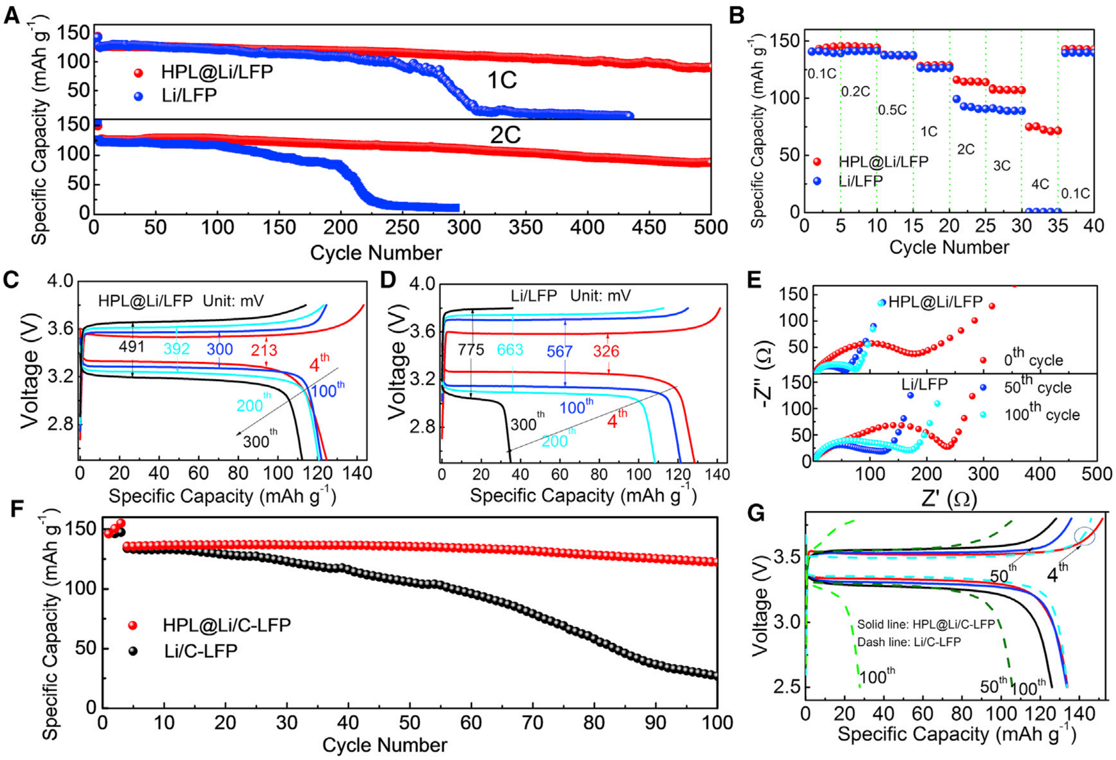

Figure 2. Electrochemical performance of full cells with HPL@Li or bare Li as anode

(A) Long-term cycling performance of HPL@Li/LFP and Li/LFP cells at current densities of 1 C and 2 C (1 C = 140 mA g^{-1}).

(B) Rate capability of the full cells at various current densities.

(C and D) Galvanostatic charge-discharge profiles of full cells at the 4th, 100th, 200th, and 300th cycle with HPL@Li and bare Li as electrode.

(E) EIS plots of the cells after various cycles.

(F) Cycling performance of HPL@Li/C-LFP and Li/C-LFP cells at a current density of 1 C.

(G) Galvanostatic charge-discharge profiles of HPL@Li/C-LFP and Li/C-LFP cells at the 4th, 50th, and 100th cycle.

The cathode used in (A)–(E) is a homemade LFP with 80 wt % active material and areal capacity ~0.8 mAh cm^{-2}. The cathode for (F) and (G) is industrial standard LFP with 96.8 wt % active material and an areal capacity of ~2 mAh cm^{-2}.

HPL@Li/HPL@Li cell, which had stable cycling performance over 1,100 h. Even at a current density of 2 mA cm^{-2}, a stable cycling performance with a cycling time of more than 800 h can still be achieved, as shown in Figure S11. These results clearly demonstrate the long-term cycling stability of the HPL@Li electrode, indicating effectiveness of the HPL in suppressing dendritic Li growth during the repeated Li^{+} plating/stripping process.

Electrochemical study of electrodes in full-cell configurations

To further evaluate the performance of the prepared HPL for Li metal anodes under practical conditions, full cells with homemade LFP cathodes and 1.0 M LiPF$_6$ in ethylene carbonate/diethyl carbonate as the electrolyte were also assembled. As displayed in Figure 2A, under a constant current density of 1 C (0.5 C for the initial 3 cycles), stable cycling performance with a capacity retention of 72%, and average CE higher than 98% over 500 cycles can be obtained for HPL@Li/LFP cells. Even at a higher current density of 2 C, a discharge capacity of 87 mAh g^{-1} (capacity retention of 70% and average CE of greater than 98%) can still be achieved after 500 cycles. In contrast, at a current density of 1 C, the Li/LFP cell shows a rapid capacity decay after 250 cycles, and at a higher current density of 2 C, a capacity retention of 50% was obtained after 209 cycles. More cell data of HPL@Li/LFP and Li/LFP cells at a current density of 1 C and 2 C are displayed in Figures S12 and S13 and Table S1, demonstrating the highly consistent electrochemical performance of assembled cells. The significant difference in electrochemical stability in HPL@Li/LFP and Li/LFP cells suggests effectiveness of HPL in stabilizing Li electrodes. The rate capability of both electrodes was evaluated as illustrated in Figure 2B. Comparable discharge capacities were obtained for both cells under low current densities; i.e., 0.1, 0.2, 0.5, and 1 C. However, significantly higher specific capacities of 114, 108, and 73 mAh g^{-1} were observed for HPL@Li/LFP cells at high current densities; i.e., 2, 3, and 4 C, respectively.

The significantly improved electrochemical performance of HPL@Li electrodes can be explained as follows. First, the protective layer efficiently suppresses Li dendrite growth, leading to less accumulation of "dead" Li. As illustrated by the charge/discharge profiles in Figure 2C and 2D, the polarization voltages of the HPL@Li electrode at the 4th, 100th, 200th, and 300th cycles are 213, 300, 392, and 491 mV, respectively, versus 326, 576, 663, and 775 mV, respectively, for bare Li electrodes. The significantly lower voltage polarization of the HPL@Li/LFP cell indicates reduced Li dendrites during the cycling process.[61] Second, the hybrid protective film contributes to a more stable SEI layer on Li metal electrodes. The electrochemical impedance spectroscopy (EIS) analysis of full cells after different cycles was used to evaluate the stability of the SEI layer on the Li metal anode (Figure 2E). Before cycling, both cells exhibit large charge-transfer resistance (R_{ct}), and after 50 and 100 cycles, decreased R_{ct} can be observed, which is attributed to activation of the electrodes. However, the R_{ct} for the bare Li electrode is much larger than that of the HPL@Li electrode, which is due to uncontrolled growth of a passivation layer on the Li surface.[62,63] The decreased R_{ct} values for the HPL@Li electrodes are beneficial for batteries to achieve a better rate capability. The CV curves of the HPL@Li/LFP full cell are displayed in Figure S14. Apart from the anodic and catholic peaks corresponding to the oxidation and reduction process between Fe^{3+} and Fe^{2+}, no other peaks are observed, indicating high electrochemical stability of HPL in the voltage window. A high Li^+ transference number (t_{Li^+}) will contribute to reduced concentration polarization and improved rate performance of batteries. As shown in Figure S15, the t_{Li^+} of HPL is calculated as 0.59 according to the potentiostatic polarization method,[64] which may contribute to the improved electrochemical performance.

High areal capacity (i.e., $\geq$2 mAh cm^{-2}) is always preferred for practical application of rechargeable LMBs, which demands even higher performance for protective layers.[65,66] However, previously reported LMBs, as shown in Table S2, always possess active LFP material around 80 wt % with an areal capacity lower than 2 mAh cm^{-2}, which is far from practical applications.[16,39,42,67–70] Here, to demonstrate the applicability of the HPL@Li electrode in high-capacity batteries, full cells with a commercial LFP cathode (C-LFP; 96.8 wt % active material, 2 mAh cm^{-2} loading based on one side of active materials; Figure S16) are also assembled for electrochemical studies. Figure 2G displays the typical charge/discharge profiles after the activation process at a current density of 0.5 C. It shows that the polarization between the charge and discharge plateaus for the HPL@Li/C-LFP cell is much lower than that for the Li/C-LFP cell, which indicates superior charge transfer kinetics of the HPL-modified Li anode. As illustrated by the galvanostatic test results in Figure 2F, at a current density of 1 C, the HPL@Li/C-LFP full cell exhibits a discharge capacity of 122 mAh g^{-1} after 100 cycles, corresponding to a capacity retention of 90% (based on the fourth cycle), which is much higher than that of the Li/C-LFP cell; i.e., 27 mAh g^{-1} with a capacity retention of only 20% after 100 cycles. As illustrated by the rate capability in Figure S17, even at a high current density of 3 C, a discharge capacity of ~86 mAh g^{-1} can still be obtained, and after resetting to 0.2 C, a high discharge capability of ~146 mAh g^{-1} was obtained, which is comparable with previous cycles at the same current density. Moreover, as shown by the comparative SEM images (Figure S18) of the bare Li electrode and HPL@Li electrode after 50 charge/discharge cycles, a uniform, dense Li layer is observed under the protective layer (Figures S18A–S18C) compared with an abundant sheet-like, porous structured Li layer along with vertically developed Li dendrites on the bare Li electrode, which can be seen in cross-sectional images (Figures S18D–S18F and S19). To better evaluate the efficiency of HPL in stabilizing the Li metal anode, the HPL@Li/LFP cell with 50 μm Li as the anode was also assembled, as shown in Figure S20. It can be seen that the HPL@Li/LFP cell shows a stable cycling performance for more than 180 cycles. Moreover, an HPL@Li/C-LFP cell was also assembled under harsh conditions (commercial LFP electrode with areal capacity of ~2 mAh cm^{-2} and weight ratio of LFP ~96.8 wt %) with 15 μL/mAh ether-based electrolyte. As shown in Figure S21, at a current density of 0.5 C, the HPL@Li/C-LFP cell shows a stable cycling performance with a capacity retention of 98% after 350 cycles. The cycling stability and excellent rate capability of the full cells with high areal capacity demonstrate that the HPL-protected Li metal electrode is highly promising for applications in pouch or cylinder batteries.

Key attributes of the HPL

Although there are many reports of constructing an efficient protective layer for stable Li metal electrodes, their key parameters have rarely been investigated systematically; this could provide insight into the underlying mechanisms and contribute to practical application of LMBs.[71] The beauty of the current designed multi-component HPL is that each component aligns with one key attribute of protective layers: cross-linked PDMS for flexibility, PEG for homogeneous ion-conducting channels, and GF for mechanical robustness. This allows further investigation of the individual role of each attribute in the protective layer via physical/electrochemical testing, numerical simulation, and morphology analysis.

The flexibility of the protective layer provided by the cross-linked PDMS affords intimate contact between the Li electrode and protective layer during the plating/stripping process, achieving enhanced electrochemical performance. The high flexibility of cross-linked PDMS was confirmed by tensile test, as shown in Figures S22 and S23; elongation before breaking is 600% versus 4% for GF and less than 1% for PEG (M_n = 2,000, semicrystalline polymer with a melting temperature of 50°C; Figure S24). The electrochemical performance agrees well with these results. As shown in Figure 3C, although the (GF+PEG)@Li/C-LFP cell exhibits improved cycling performance compared with the Li/C-LFP cell, it still shows unsatisfactory electrochemical performance with a discharge capacity of only 56 mAh g^{-1} after 100 cycles in comparison with 122 mAh g^{-1} for the HPL@Li/C-LFP cell, which emphasizes the importance of flexibility provided by cross-linked PDMS. As shown by the SEM images in Figure 4C, 4H, and 4M, (GF+PEG)@Li electrodes show that the Li layer and protective film are relatively loose and that the protective layer can even be deformed, losing contact with the Li metal, which is in contrast with the dense Li electrode and intimate contact between the protective layer and Li electrode of the HPL@Li electrode (Figures 4B, 4G, and 4L). The EIS results of the symmetric cells show that although the initial R_s, R_{sei} and R_{ct} values of the cell with HPL@Li as electrodes are higher than those of the cell with bare Li or (GF+PEG)@Li as electrodes (Figures 3D–3H; Table S3), they decreased to levels that are lower than those of bare Li and (GF+PEG)@Li cells after 100 h. This phenomenon is consistent with the Li^+ plating/stripping overpotential results in symmetric cell tests (Figures 1 and S10). The lower impedance of the HPL@Li/HPL@Li cell suggests formation of a stable SEI layer during the Li^+ plating/stripping

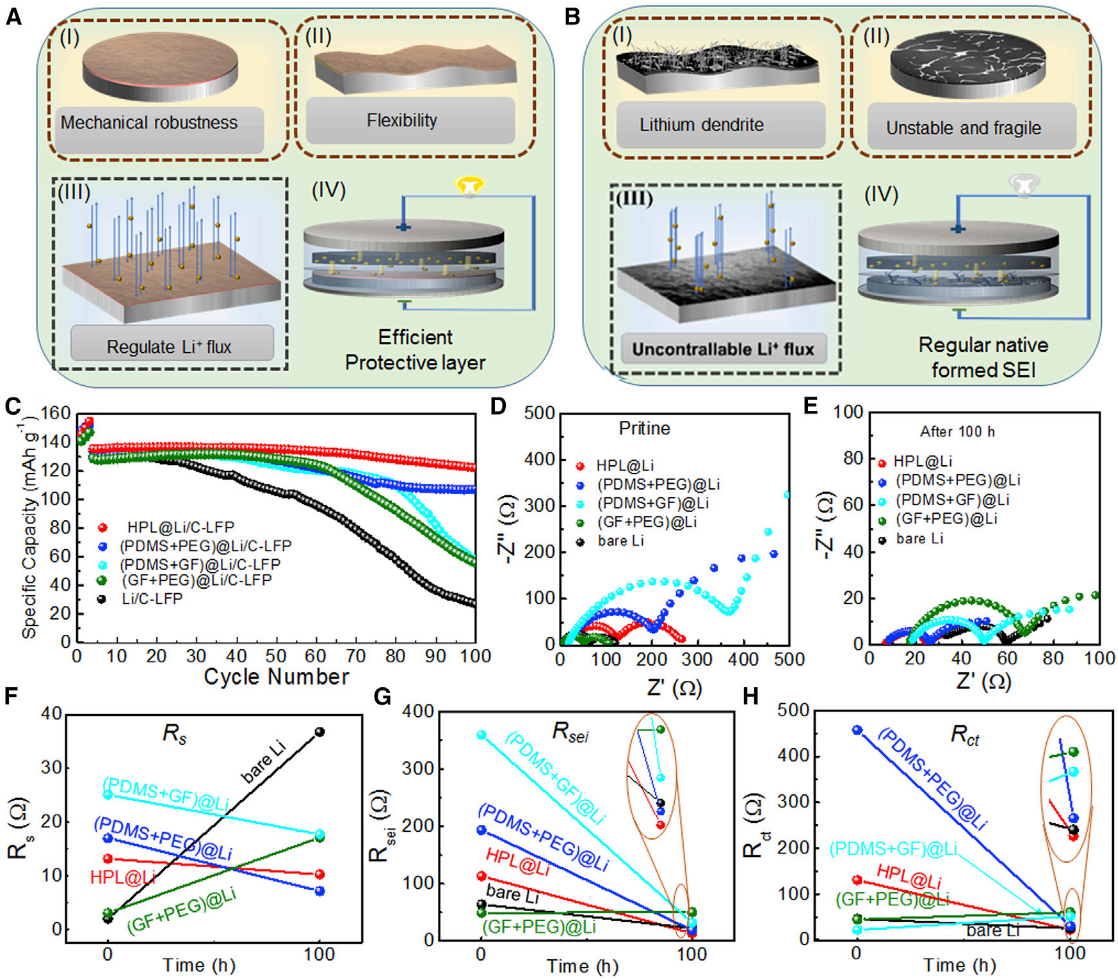

Figure 3. Schematic and electrochemical performance of cells with efficient protective layers and regular native formed SEI films

(A and B) Comparative characteristics of efficient protective layers and regular native formed SEI films.

(C) Cycling performance of cells with different types of Li anodes.

(D and E) EIS profiles of symmetric cells with different Li electrodes before and after cycling for 100 h, respectively.

(F–H) Fitted EIS result variation before and after cycling for 100 h for symmetric cells with different electrodes (R_s, R_{sei}, and R_{ct} represent the resistance of electrolyte, the resistance of the interphase on the surface of the electrode, and charge transfer resistance, respectively).

process. The larger impedance of the cell with bare Li as electrodes arise from accumulation of "dead" Li, which increases the interfacial area and thickness of the SEI film. The gradual decrease in voltage polarization and impedance suggests an "activation" process of the HPL layer during the cycling process, which may be caused by infiltration of the electrolyte and potential side reactions. Overall, the high flexibility provided by the cross-linked PDMS can better accommodate the volume fluctuation during the cycling process, and the protective layer with reduced flexibility cannot effectively regulate Li^+ deposition, resulting in accumulation of "dead" Li and, hence, poor electrochemical performance.[60]

Providing homogeneous ion-conducting channels is another essential parameter for protective layer design on Li metal electrodes that can contribute to superior charge transfer kinetics and reduced local flux of Li^+, leading to dendritic-free Li metal anodes.[69,72–74] To better understand their functionality in affecting electrochemical performance, as shown in Figure S25 and Table S3, the ionic conductivities of

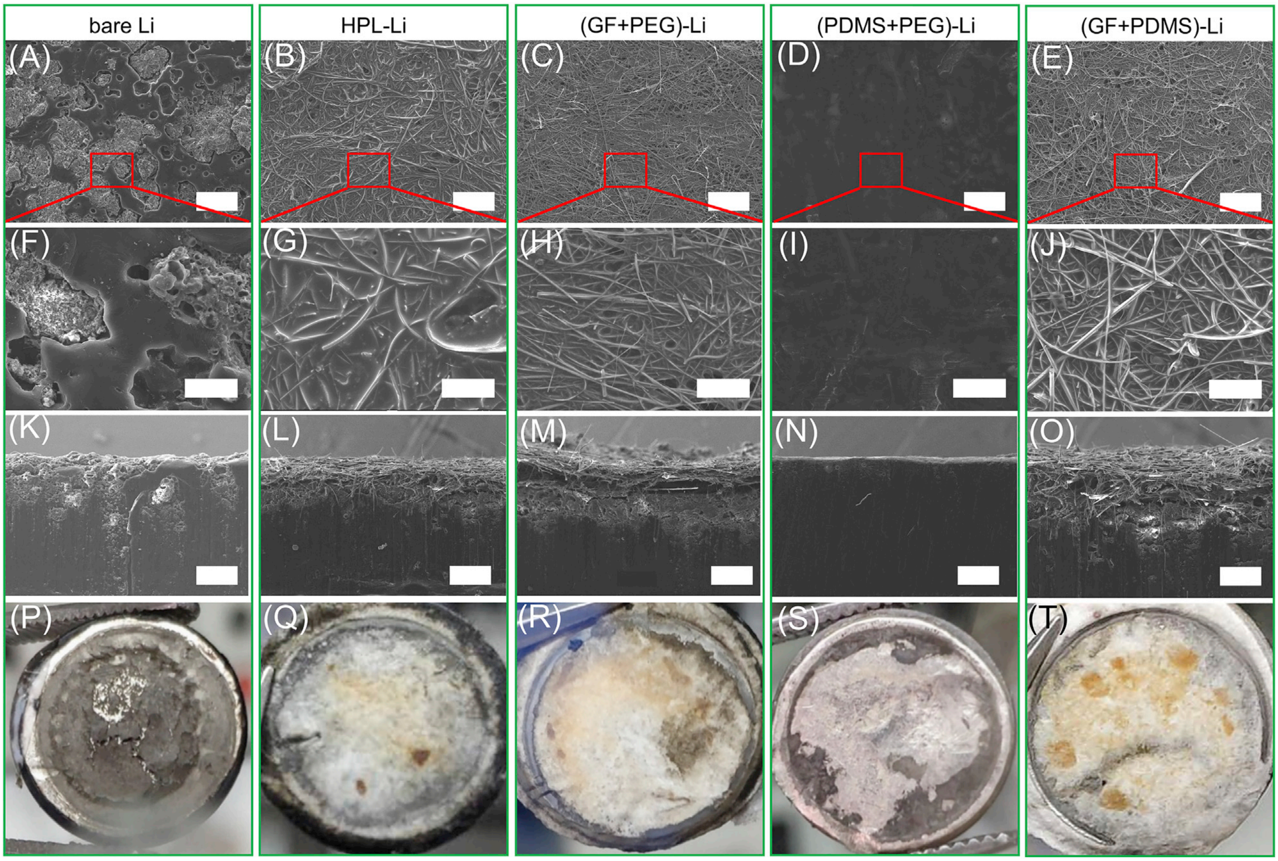

Figure 4. Surface morphology of bare Li and modified Li after 50 cycles

(A–E) SEM images of Li electrodes with different protective layers.

(F–I) Magnified images of (A)–(E), respectively.

(K–O) Cross-sectional images of Li electrodes with different protective layers.

(P–T) Photographs of Li electrodes with different protective layers.

The scale bars in (A)–(E), (K)–(O), and (F)–(J) represent 200, 100, and 50 μm, respectively.

different components are studied individually. The PEG+GF shows the highest ionic conductivity of 1.1 × 10^{-5} S/cm, which is an order of magnitude higher than that of PDMS+GF, indicating a role of PEG in providing Li^+-conducting channels. For HPL, the ionic conductivity is lower than that of PEG+GF but higher than that of PDMS+GF, and the results are consistent with the cycling performance. As shown in Figure 3C, after removing the PEG component, the (GF+PDMS)@Li/C-LFP cell displays better cycling stability than the Li/C-LFP cell (capacity retention of 42% versus 20% after 100 cycles) but much lower capacity retention than the HPL@Li/C-LFP cell (capacity retention of 90% under the same condition). The lower ionic conductivity of the protective layer without PEG was also confirmed by the EIS results of symmetric cells; without the efficient ionic conducting component that allows homogeneous Li^+-conducting channels, as shown in Figures 3F–3H and Table S3, the cell with (GF+PDMS)@Li as electrodes displays much higher R_{sei} and R_{ct} values than cells with HPL@Li as electrodes after cycling for 100 h. Moreover, the reduced ion-conducting channels of the protective layer may increase the local Li^+ flux near the dendrite tips,[73] and comparative SEM images of the (GF+PDMS)@Li electrode (rough surface; Figures 4E, 4J, and 4T) and the HPL@Li electrode (smooth surface; Figures 4B, 4J, and 4Q) after 50 cycles also partially confirm this assumption. As shown, the (GF+PDMS)@Li electrode reveals more disordered surface

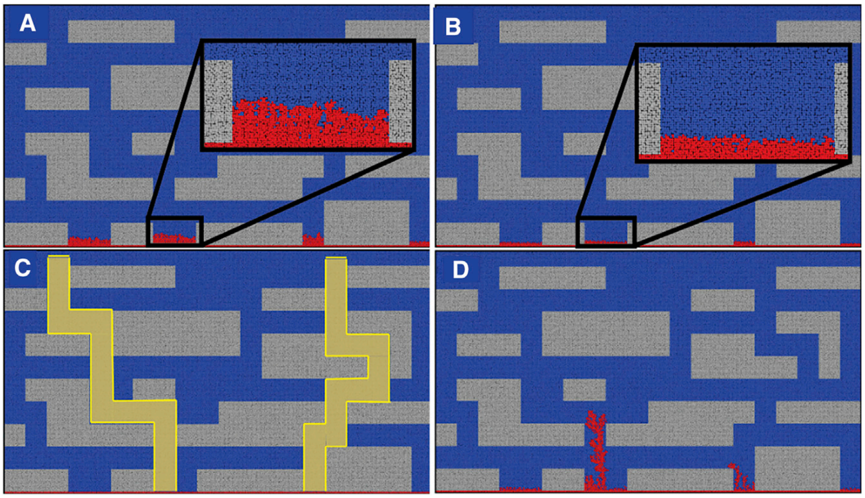

Figure 5. Simulations of Li^+ conducting channels and dendrite growth with mass transport in the blue regions, the GF as the gray regions, and the anode and subsequent dendrite growth shown in red

(A) The higher ion transport (5 $\mu m^2\ s^{-1}$) that represents the HPL with the PEG component.

(B) The lower ion transport (3.3 $\mu m^2\ s^{-1}$) that represents the (GF+PDMS) layer.

(C and D) The Li^+-conducting channels (yellow regions, 15 $\mu m^2\ s^{-1}$) in the bulk ion-conducting (3.3 $\mu m^2\ s^{-1}$) PDMS, which leads to non-uniform Li^+ transport and dendrite growth (D).

All simulation data were taken at the same time.

morphologies, which can also be seen in the computational modeling of the interface discussed below. Its cross-sectional image (Figure 4O) even shows some vertically extended "dead" Li, which is in contrast with the smooth surface of the HPL@Li electrode after the same electrochemical process.

Computational modeling of the electrode-electrolyte interface was used to further understand the effects of PEG on performance of the protective layer. Here, a previously published model of dendrite growth using the smoothed particle hydrodynamics (SPH) method was used.[75–77] Three scenarios were considered: one representing a homogeneous mixture of PDMS, PEG, and GF; one with only PDMS and GF; and one with imperfect mixing of PDMS and GF. As shown in Figure 5, the domain for the simulations is a region near the electrode-protective layer interface; the electrode is at the bottom of the image, and Li^+ deposition and dendrite growth are shown in red. In the first two scenarios, the GF (gray) is surrounded by a uniform conductive medium (blue regions), as shown in Figures 5A and 5B. The GF (gray regions) is modeled explicitly in the simulation, and the dimensions are chosen to match the diameter of GF used in the experiments. The dominant orientation of GF is parallel to the anode surface and shown as such in the simulation. A high ionic conductivity (5.0 $\mu m^2\ s^{-1}$) is shown in Figure 5A to represent the HPL (PDMS, PEG, and GF), and a low ionic conductivity (3.3 $\mu m^2\ s^{-1}$) is shown in Figure 5B to represent PDMS and GF. In the final scenario, high conductivity pathways are placed in the blue regions to represent non-uniformities in the PDMS, such as a channel or gap; these are indicated by yellow shaded regions in Figure 5C. The channels have a higher ion conductivity than the bulk regions (blue, Figure 5C), which create non-uniform ionic transport and dendrite growth. The simulations (Figure 5) show that the lower Li^+ transport through the (GF+PDMS) layer cannot solely explain the lower cycling stability and more disordered surface morphology seen experimentally. As shown in Figure 5, if the ion conducting channels are less but uniform (Figure 5B), then Li^+ deposition is still relatively uniform, similar to what is seen when the protective layer includes PEG (Figure 5A) and has a high Li^+ transport rate. A possible reason for the non-uniform Li^+ transport is formation of localized channels (Figure 5C) around the GF. For HPL@Li, the presence of PEG will allow relatively homogeneous Li^+-conducting channels, which reduces the localized Li^+ flux in specific channels. For the (GF+PDMS)@Li electrode under the same or higher charge/discharge current density, less and localized ion transfer channels will render high Li^+ flux in specifics channels, leading to non-uniform deposition of Li on the anode surface and reduced cycling stability. Evidence of this is shown in Figure 5D, where the dendrites grown are similar to those seen when LMBs have failed[78] and agree with the experimental results of Figure 4.

In addition to the flexibility and homogeneous ion-conducting channels, mechanical strength also plays an important role in protective layers. A higher Young's modulus of protective layers is essential to maintain structural integrity during the Li plating/stripping processes, especially at high current density, which will reduce side reactions with the fresh exposed interface and electrolyte consumption.[45] In the current system, the GF provides high mechanical strength for the HPL. As shown by the tensile result of GF in Figure S23, the ultimate tensile stress was measured as ~14 MPa, much larger than that of cross-linked PDMS (~1.5 kPa) and PEG (too brittle for a tensile test). The electrochemical performance also confirmed this presumption. As shown in Figure 3C, the cycling performance indicates that, with the GF-reinforced polymeric film as the protective layer, the cells with (GF+PDMS)@Li, (GF+PEG)@Li, and HPL@Li as anodes exhibited improved electrochemical performance compared with the cell with bare Li as the anode. With reduced mechanical robustness, the cell with (PDMS+PEG)@Li displays slightly lower capacity retention than the cell with HPL@Li as the electrode (82% versus 90% after 100 cycles). The SEM images of the (PDMS+PEG)@Li electrode after 50 cycles (Figures 4D, 4I, 4N, and 4S) also show a relatively smooth surface and clear cross-sectional morphologies. This demonstrates that the protecting layer composed of PDMS and PEG can still suppress dendritic Li growth in a relatively short-term cycling process (the initial 50 cycles here). However, without robust mechanical support from inorganic fillers, the polymeric film is mechanically too weak to efficiently prevent micro-penetration of Li dendrites after the long-term cycling process, leading to slight capacity fading, as shown in Figure 3C. This result is consistent with the EIS results of symmetric cells in Figure 3, where the R_{sei} and R_{ct} values of the cell with (PDMS+PEG)@Li as electrodes are slightly higher than that of the cell with HPL@Li as electrodes, suggesting an unstable Li electrode after the long-term (100 h in this study) cycling process. The phenomenon agrees well with previous reports showing that an inorganic filler could enhance the mechanical robustness of polymeric protective films, suppress Li dendrite growth, and maintain structural integrity, especially under high current density (high areal capacity) and the long-term cycling process.[70,79]

In summary, we report a rationally designed GF-reinforced polymeric layer that allows a Li metal electrode with stable cycling performance. The role of each key attribute of HPL (i.e., flexibility, homogeneous ion-conducting channels, and mechanical robustness) is isolated and investigated via a series of electrochemical, physical, and numerical experiments. With synergistic effects of different attributes, cells with HPL-modified electrodes exhibit significantly improved electrochemical performance in Li/HPL@Cu half cells, HPL@Li/HPL@Li symmetric cells, and HPL@Li/LFP full cells compared with cells using a bare Cu or Li electrode. Even with the industrial standard LFP as the cathode, a discharge capacity of 122 mAh g^{-1} after 100 cycles (capacity retention of 90%) can still be achieved. More importantly, after investigating the role of each component of the HPL, we found that all three key attributes play important roles in stabilizing the Li metal anode: the improved flexibility makes the HPL better able to accommodate volume fluctuation; the homogeneous ion-conducting channels contribute to superior charge transfer kinetics and drastically reduced local flux heterogeneity of Li^+, which are vital to achieve dendrite-free Li metal anodes; and the enhanced mechanical robustness can maintain structural integrity of the protective layer during the Li^+ plating/stripping process, especially at high current density and long-term cycling. Additionally, detailed computational modeling of the protective layer-electrode interface showed that imperfections at the interface between the PDMS and GF can lead to non-uniform Li^+ mass flux and dendrite growth, which reinforces and expands the experimental results.

This work not only reports an easily fabricated, low-cost, high-performance HPL for Li metal electrodes but also provides deep insight into the key attributes of the protective layer for Li metal electrodes, which sheds light on the design principles of constructing effective protecting layers for practical chargeable LMBs with high energy density and prolonged cycle life.

EXPERIMENTAL PROCEDURES

Resource availability

Lead contact

Further information and requests for resources should be directed to and will be fulfilled by the lead contact, Dr. Peng-Fei Cao (caop@ornl.gov).

Materials availability

Reagents generated in this study will be made available upon request, but we may require a payment and/or a completed materials transfer agreement if there is potential for commercial application.

Data and code availability

The authors declare that the data supporting the findings are available within the article and the supporting information. All other data are available from the lead contact upon reasonable request.

Preparation of cross-Linked PDMS

The cross-linked PDMS was prepared as follows. 25.22 mg (0.12 mmol) of BCA (Tianjin Heowns Biochemical Technology) was dissolved in 2,500 mg of toluene and stirred. Then 500 mg (0.1 mmol) of PDMS-NH_2 (Gelest) was added to the solution. Then it was purged with nitrogen (N_2) flow for 10 min, and the reaction was continued for 2 h at 80°C under magnetic stirring. After that, 100 mg of multi-amine functionalized PDMS (~48 amine groups per molecule, Gelest) in toluene (12 wt %) was added to the solution, and the reaction was continued for another 2 h under the same reaction conditions.

Characterization

The morphology of bare and modified electrodes was observed by SEM (JSM-7800, JEOL, Japan). TGA was performed with a TG-DTA8122 instrument at a scanning rate of 10°C/min under a N_2 atmosphere. The T_g of cross-linked PDMS was measured by temperature-modulated DSC (TA Instruments, DSC 2500) in a temperature range of −150°C–150°C. Fourier transform IR (FTIR) spectra were recorded on a Nicolet iS50 FTIR spectrometer (Bruker Tensor II) with a scanning range of 400–4,000 cm^{-1}. Rheology measurements of PDMS were carried out on an AR2000ex rheometer (TA Instruments) using 4-mm plates. Tensile analysis was performed using a TA Instruments RSA-G2 Solid Analyzer. Samples were elongated at a rate of 0.1 mm/s until breaking. The reported tensile properties were an average of a minimum of three samples. The ionic conductivity of the films was evaluated by EIS. Symmetric cells were utilized for the measurements, consisting of two identical stainless steel foils as blocking electrodes and a polymer membrane sandwiched in between. The ionic conductivity (σ) is calculated based on the equation

$$\sigma = \frac{L}{R_b S},$$

where L (cm), R_b, and S are the film thickness, ohmic resistance (Ω), and contact area (cm^2), respectively.

The Li^+ transference number was obtained via the potentiostatic polarization method. Typically, a symmetric HPL@Li/HPL@Li cell was assembled, and subsequently the polarization currents under a small polarization potential were recorded. The initial and steady-state values of the bulk resistances (R_0 and R_s) were measured by EIS before and after potentiostatic polarization. The t_{Li^+} was calculated according to the following equation:

$$t_{Li^+} = \frac{I_s\ (\Delta V - I_0 R_0)}{I_0 (\Delta V - I_s R_s)},$$

where I_0 and I_s are the initial and steady-state current values, respectively, and R_0 and R_s are the initial and steady-state electrode/electrolyte interfacial resistances, respectively.

Fabrication of HPL@Cu and HPL@Li electrodes

The HPL@Cu and HPL@Li electrodes were prepared by dripping the polymer solution on Cu foil or the Li metal surface and then coated with GF (Whatman, grade GF/D) in an argon-filled glovebox. After drying in a vacuum oven for 12 h, the HPL-Cu and HPL-Li electrodes were obtained. The (PDMS+PEG)-Li, (GF+PDMS)-Li, (GF+PEG)-Li and GF-Li electrodes were prepared using a similar procedure.

Preparation of homemade LFP cathodes

To fabricate the LFP electrode (homemade), LFP (HF-Kejing), acetylene black (TIMICAL SUPER C65), and PVDF difluoride (Kynar HSV900, ARKEMA) with a weight ratio of 8:1:1 were suspended in N-methylpyrrolidinon to obtain a slurry. After stirring for 12 h, the slurry was then coated onto Al foil and dried at 120°C for 12 h in a vacuum. The electrode was cut into circular disks with a diameter of 13.0 mm, and the mass loading of the electrode was ~5 mg cm^{-2}. The commercial LFP electrode was provided by the battery company and was double-coated with active materials. Before being used in CR2032-type cells, one side of the active material was corroded with *N*, *N*-dimethylformamide. After drying in a vacuum oven, the electrode was punched into circular disks with a diameter of 13.0 mm.

Battery assembly and electrochemical measurements

The electrodes were cut into a 1.32-cm^2 circular sheet to assemble the CR2032 coin cells in an argon-filled glove box with O_2 and H_2O levels lower than 1 ppm. The half cells were assembled with bare Cu or HPL@Cu as working electrode and Li metal as counter electrode. The symmetric cells were assembled with configurations of bare Li/separator/bare Li or HPL@Li/Separator/HPL-Li. The full cells were assembled with LFP (homemade or commercial) as cathode and bare Li or modified Li (HPL@Li, (PDMS+PEG)@Li, (GF+PDMS)@Li, (GF+PEG)@Li and GF@Li) as anode. In all cells, Celgard 2400 polypropylene membranes were used as separators. For half and symmetric cells, the electrolyte consisted of 1 M Li bis(trifluoromethanesulfonyl)imide in 1,3-dioxolane/dimethyl ether (v/v = 1:1) with 2 wt % $LiNO_3$ as an additive. For full cells, 1 M $LiPF_6$ in ethylene carbonate/diethyl carbonate (1: 1 by volume) solution was used as electrolyte. The galvanostatic test was performed by using the LAND CT2001A battery test system. EIS was performed on the Zennium Pro Electrochemical System with a scanning speed of 0.1 $mV\ s^{-1}$ and a frequency range of 10^{-1}–10^4 Hz at a 5-mV amplitude. All electrochemical results were obtained at 25°C in a temperature-controlled chamber.

Interfacial mesoscale modeling

SPH is a meshless Lagrangian method that discretizes the domain with discrete particles that carry their properties (density, species concentration, etc.) with them. SPH was used because of its convenience in modeling the moving, deformable boundaries and surface reactions associated with the dendrite growth phenomenon. Its particle nature allows easy implementation of surface phenomena and implicit boundary tracking without the need for any level set or front tracking methods. The partial differential equations of the system, including mass and species conservation and surface reactions, are discretized in time and space using the SPH method.[80] The model domain includes the anode surface, the HPL, dendrite structures, and a finite diffusion boundary layer. Li ions diffuse to the anode surface, where they react with electrons and form dendrite structures. The surfaces of the dendrite structures will become the new boundaries for future dendrite growth, whereas the interior structure will become embedded and no longer contributes to future reactions. The thickness of the diffusion layer is based on data from the literature on experimental results.[81] Outside of the diffusion layer, we assumed that the ion concentration is equal to the concentration of bulk solution. The simulations focus on the reactive mass transport near the anode-electrolyte interface and do not model a complete battery, potential and electro-convection effects, or secondary reactions. These simplifications are done to isolate the critical effects of ionic transport and the reactive anode interface during charge conditions on dendritic growth.

The species conservation equation is

$$\frac{\partial C(x,y,t)}{\partial t} = \nabla\cdot\left(D\nabla C(x,y,t)\right),\ \ \vec{r}\in\Omega_F \qquad \text{(Equation 1)}$$

where Ω_F is the fluid domain (electrolyte solution), D is the diffusivity (or conductivity), and C is the Li^+ concentration. At the reactive anode surface, a first-order reaction boundary condition is applied,

$$D\nabla c_i\left(\vec{r_s}\,,\ t\right) = K\left(c\left(\vec{r_s}\,,\ t\right) - C_{eq}\right),\ \ \vec{r_s}\in\Gamma,\ \ t>0, \qquad \text{(Equation 2)}$$

where $\vec{r_s}$ is a point along the reactive surface Γ, C_{eq} is the equilibrium concentration for the solidification reaction, and K is the reaction rate coefficient. The surfaces of the dendrite structures will become the new boundaries for future dendrite growth, whereas the interior structure will be embedded and no longer contributes to future reactions. The thickness of the diffusion layer is based on data from the literature on experimental results. A uniform initial concentration is assumed throughout the domain and a constant concentration (C_1) outside of the diffusion layer for the duration of the simulation,

$$C(x, y = L, t) = C_1. \qquad \text{(Equation 3)}$$

The simulations focus on the reactive mass transport near the anode-electrolyte interface and do not model a complete battery, the potential and electro-convection effects, or secondary reactions. These simplifications are done to isolate the critical effects of ionic transport and the reactive anode interface during charge conditions on dendritic growth.

SUPPLEMENTAL INFORMATION

Supplemental information can be found online at https://doi.org/10.1016/j.xcrp.2021.100534.

ACKNOWLEDGMENTS

S. Gao, F.S., Y.P., and H.Y. are supported by the Natural Science Foundation of China (21421001), the Natural Science Foundation of Tianjin, China (18JCZDJC31400), and the MOE Innovation Team (IRT13022). P.-F.C. and A.P.S. acknowledge financial support from the US Department of Energy, Office of Science, Basic Energy Science, Material Science, and Engineering Division. A.C. and E.R. acknowledge partial financial support from the National Science Foundation through grant 1727316 and 2034154.

AUTHOR CONTRIBUTIONS

Conceptualization, S. Gao., P-F.C., and H.Y.; methodology, S. Gao., P.-F.C., and H.Y.; software, A.C. and E.R.; Investigation, S. Gao, Y.P., D.Y., S. Ge, and A.P.S.; writing – original draft, S. Gao, F.S., P.-F.C., and H.Y.; writing – review & editing, S. Gao, A.C., F.S., Y.P., D.Y., E.R., H.Y., and P.-F.C.; supervision, H.Y. and P.-F.C.; funding acquisition, H.Y., P.-F.C., A.C., and E.R.

DECLARATION OF INTERESTS

The authors declare no competing interests.

Received: April 1, 2021
Revised: June 22, 2021
Accepted: July 21, 2021
Published: August 6, 2021

REFERENCES

1. Zhu, J., Zhu, P., Yan, C., Dong, X., and Zhang, X. (2019). Recent Progress in Polymer Materials for Advanced Lithium-Sulfur Batteries. Prog. Polym. Sci. *90*, 118–163.
2. Yu, Z., Cui, Y., and Bao, Z. (2020). Design Principles of Artificial Solid Electrolyte Interphases for Lithium-Metal Anodes. Cell Rep. Phys. Sci. *1*, 100119.
3. Ma, L., Fu, C., Li, L., Mayilvahanan, K.S., Watkins, T., Perdue, B.R., Zavadil, K.R., and Helms, B.A. (2019). Nanoporous Polymer Films with a High Cation Transference Number Stabilize Lithium Metal Anodes in Light-Weight Batteries for Electrified Transportation. Nano Lett. *19*, 1387–1394.
4. Cheng, X.-B., Yan, C., Zhang, X.-Q., Liu, H., and Zhang, Q. (2018). Electronic and Ionic Channels in Working Interfaces of Lithium Metal Anodes. ACS Energy Lett. *3*, 1564–1570.
5. Feng, Y., Zhang, C., Jiao, X., Zhou, Z., and Song, J. (2020). Highly stable lithium metal anode with near-zero volume change enabled by capped 3D lithophilic framework. Energy Storage Mater. *25*, 172–179.
6. Feng, Y., Zhang, C., Li, B., Xiong, S., and Song, J. (2019). Low-volume-change, dendrite-free lithium metal anodes enabled by lithophilic 3D matrix with LiF-enriched surface. J. Mater. Chem. A Mater. Energy Sustain. *7*, 6090–6098.
7. Mukhopadhyay, A., and Jangid, M.K. (2018). Li metal battery, heal thyself. Science *359*, 1463, 1463.
8. Yin, X., Tang, W., Jung, I.D., Phua, K.C., Adams, S., Lee, S.W., and Zheng, G.W. (2018). Insights into morphological evolution and cycling behaviour of lithium metal anode under mechanical pressure. Nano Energy *50*, 659–664.
9. Cheng, X.-B., Huang, J.-Q., and Zhang, Q. (2018). Review-Li Metal Anode in Working Lithium-Sulfur Batteries. J. Electrochem. Soc. *165*, A6058–A6072.
10. Albertus, P., Babinec, S., Litzelman, S., and Newman, A. (2018). Status and Challenges in Enabling the Lithium Metal Electrode for High-Energy and Low-Cost Rechargeable Batteries. Nat. Energy *3*, 16–21.
11. Zhu, P., Zhu, J., Zang, J., Chen, C., Lu, Y., Jiang, M., Yan, C., Dirican, M., Selvan, R.K., and Zhang, X. (2017). A Novel Bi-functional Double-Layer rGO-PVDF/PVDF Composite Nanofiber Membrane Separator with Enhanced Thermal Stability and Effective Polysulfide Inhibition for High-Performance Lithium-Sulfur Batteries. J. Mater. Chem. A Mater. Energy Sustain. *5*, 15096–15104.
12. Zheng, G., Lee, S.W., Liang, Z., Lee, H.-W., Yan, K., Yao, H., Wang, H., Li, W., Chu, S., and Cui, Y. (2014). Interconnected hollow carbon nanospheres for stable lithium metal anodes. Nat. Nanotechnol. *9*, 618–623.
13. Zuo, T.-T., Yin, Y.-X., Wang, S.-H., Wang, P.-F., Yang, X., Liu, J., Yang, C.-P., and Guo, Y.-G. (2018). Trapping Lithium into Hollow Silica Microspheres with a Carbon Nanotube Core for Dendrite-Free Lithium Metal Anodes. Nano Lett. *18*, 297–301.
14. Wu, N., Shi, Y.-R., Jia, T., Du, X.-N., Yin, Y.-X., Xin, S., and Guo, Y.-G. (2019). Green *in Situ* Growth Solid Electrolyte Interphase Layer with High Rebound Resilience for Long-Life Lithium Metal Anodes. ACS Appl. Mater. Interfaces *11*, 43200–43205.
15. Cui, X., Chu, Y., Qin, L., and Pan, Q. (2018). Stabilizing Li Metal Anodes through a Novel

Self-Healing Strategy. ACS Sustain. Chem.& Eng. *6*, 11097–11104.

16. Xu, R., Xiao, Y., Zhang, R., Cheng, X.-B., Zhao, C.-Z., Zhang, X.-Q., Yan, C., Zhang, Q., and Huang, J.-Q. (2019). Dual-Phase Single-Ion Pathway Interfaces for Robust Lithium Metal in Working Batteries. Adv. Mater. *31*, e1808392.

17. Sun, W., Zhang, J., Xie, M., Lu, D., Zhao, Z., Li, Y., Cheng, Z., Zhang, S., and Chen, H. (2020). Ultrathin Aramid/COF Heterolayered Membrane for Solid-State Li-Metal Batteries. Nano Lett. *20*, 8120–8126.

18. Zhou, D., Tkacheva, A., Tang, X., Sun, B., Shanmukaraj, D., Li, P., Zhang, F., Armand, M., and Wang, G. (2019). Stable Conversion Chemistry-Based Lithium Metal Batteries Enabled by Hierarchical Multifunctional Polymer Electrolytes with Near-Single Ion Conduction. Angew. Chem. Int. Ed. Engl. *58*, 6001–6006.

19. Li, S., Zhang, S.-Q., Shen, L., Liu, Q., Ma, J.-B., Lv, W., He, Y.-B., and Yang, Q.-H. (2020). Progress and Perspective of Ceramic/Polymer Composite Solid Electrolytes for Lithium Batteries. Adv. Sci. (Weinh.) *7*, 1903088.

20. Yao, Y.-X., Chen, X., Yan, C., Zhang, X.-Q., Cai, W.-L., Huang, J.-Q., and Zhang, Q. (2021). Regulating Interfacial Chemistry in Lithium-Ion Batteries by a Weakly Solvating Electrolyte. Angew. Chem. Int. Ed. Engl. *60*, 4090–4097.

21. Zhang, W., Tu, Z., Qian, J., Choudhury, S., Archer, L.A., and Lu, Y. (2018). Design Principles of Functional Polymer Separators for High-Energy, Metal-Based Batteries. Small *14*, e1703001.

22. Selvan, R.K., Zhu, P., Yan, C., Zhu, J., Dirican, M., Shanmugavani, A., Lee, Y.S., and Zhang, X. (2018). Biomass-derived porous carbon modified glass fiber separator as polysulfide reservoir for Li-S batteries. J. Colloid Interface Sci. *513*, 231–239.

23. Li, T., Liu, H., Shi, P., and Zhang, Q. (2018). Recent Progress in Carbon/Lithium Metal Composite Anode for Safe Lithium Metal Batteries. Rare Met. *37*, 449–458.

24. Shen, L., Shi, P., Hao, X., Zhao, Q., Ma, J., He, Y.-B., and Kang, F. (2020). Progress on Lithium Dendrite Suppression Strategies from the Interior to Exterior by Hierarchical Structure Designs. Small *16*, e2000699.

25. Hong, S.H., Jung, D.H., Kim, J.H., Lee, Y.H., Cho, S.J., Joo, S.H., Lee, H.W., Lee, K.S., and Lee, S.Y. (2020). Electrical Conductivity Gradient Based on Heterofibrous Scaffolds for Stable Lithium-Metal Batteries. Adv. Funct. Mater. *30*, 1908868.

26. Wang, Z., Wang, Y., Zhang, Z., Chen, X., Lie, W., He, Y.-B., Zhou, Z., Xia, G., and Guo, Z. (2020). Building Artificial Solid-Electrolyte Interphase with Uniform Intermolecular Ionic Bonds toward Dendrite-Free Lithium Metal Anodes. Adv. Funct. Mater. *30*, 2002414.

27. Xu, R., Cheng, X.-B., Yan, C., Zhang, X.-Q., Xiao, Y., Zhao, C.-Z., Huang, J.-Q., and Zhang, Q. (2019). Artificial Interphases for Highly Stable Lithium Metal Anode. Matter *1*, 317–344.

28. Qi, L., Wu, Z., Zhao, B., Liu, B., Wang, W., Pei, H., Dong, Y., Zhang, S., Yang, Z., Qu, L., and Zhang, W. (2020). Advances in Artificial Layers for Stable Lithium Metal Anodes. Chemistry *26*, 4193–4203.

29. Zhang, S.-J., Gao, Z.-G., Wang, W.-W., Lu, Y.-Q., Deng, Y.-P., You, J.-H., Li, J.-T., Zhou, Y., Huang, L., Zhou, X.-D., and Sun, S.G. (2018). A Natural Biopolymer Film as a Robust Protective Layer to Effectively Stabilize Lithium-Metal Anodes. Small *14*, e1801054.

30. Zhang, X., Xie, Z., and Zhou, Z. (2019). Recent Progress in Protecting Lithium Anodes for Li-O_2 Batteries. ChemElectroChem *6*, 1969–1977.

31. Lopez, J., Mackanic, D.G., Cui, Y., and Bao, Z. (2019). Designing Polymers for Advanced Battery Chemistries. Nat. Rev. Mater. *4*, 312–330.

32. Lee, H., Lee, D.J., Kim, Y.-J., Park, J.-K., and Kim, H.-T. (2015). A Simple Composite Protective Layer Coating that Enhances the Cycling Stability of Lithium Metal Batteries. J. Power Sources *284*, 103–108.

33. Lee, Y.M., Choi, N.-S., Park, J.H., and Park, J.-K. (2003). Electrochemical Performance of Lithium/Sulfur Batteries with Protected Li Anodes. J. Power Sources *119-121*, 964–972.

34. Yang, C., Fu, K., Zhang, Y., Hitz, E., and Hu, L. (2017). Protected Lithium-Metal Anodes in Batteries: From Liquid to Solid. Adv. Mater. *29*, 1701169.

35. Gao, Y., Zhao, Y., Li, Y.C., Huang, Q., Mallouk, T.E., and Wang, D. (2017). Interfacial Chemistry Regulation *via* a Skin-Grafting Strategy Enables High-Performance Lithium-Metal Batteries. J. Am. Chem. Soc. *139*, 15288–15291.

36. Wang, X., Pan, Z., Zhuang, J., Li, G., Ding, X., Liu, M., Zhang, Q., Liao, Y., Zhang, Y., and Li, W. (2019). Simultaneously Regulating Lithium Ion Flux and Surface Activity for Dendrite-Free Lithium Metal Anodes. ACS Appl. Mater. Interfaces *11*, 5159–5167.

37. Sun, Y., Zhao, Y., Wang, J., Liang, J., Wang, C., Sun, Q., Lin, X., Adair, K.R., Luo, J., Wang, D., et al. (2019). A Novel Organic "Polyurea" Thin Film for Ultralong-Life Lithium-Metal Anodes *via* Molecular-Layer Deposition. Adv. Mater. *31*, e1806541.

38. Kwak, W.-J., Park, J., Trung Thien, N., Kim, H., Byon, H.R., Jang, M., and Sun, Y.-K. (2019). A Dendrite- and Oxygen-Proof Protective Layer for Lithium Metal in Lithium-Oxygen Batteries. J. Mater. Chem. A Mater. Energy Sustain. *7*, 3857–3862.

39. You, J.-H., Zhang, S.-J., Deng, L., Li, M.-Z., Zheng, X.-M., Li, J.-T., Zhou, Y., Huang, L., and Sun, S.-G. (2019). Suppressing Li dendrite by a Protective Biopolymeric Film from Tamarind Seed Polysaccharide for High-Performance Li Metal Anode. Electrochim. Acta *299*, 636–644.

40. Chang, C.-H., Chung, S.-H., and Manthiram, A. (2017). Dendrite-Free Lithium Anode *via* a Homogenous Li-Ion Distribution Enabled by a Kimwipe Paper. Adv. Sustainable Syst. *1*, 1600034.

41. Bai, P., Li, J., Brushett, F.R., and Bazant, M.Z. (2016). Transition of lithium growth mechanisms in liquid electrolytes. Energy Environ. Sci. *9*, 3221–3229.

42. Zhang, W., Zhuang, H.L., Fan, L., Gao, L., and Lu, Y. (2018). A "cation-anion regulation" synergistic anode host for dendrite-free lithium metal batteries. Sci. Adv. *4*, eaar4410.

43. Kim, S., Park, J., Friesen, A., Lee, H., Lee, Y.M., and Ryou, M.-H. (2018). Composite Protection Layers for Dendrite-Suppressing Non-Granular Micro-Patterned Lithium Metal Anodes. Electrochim. Acta *282*, 343–350.

44. Jiang, S., Lu, Y., Lu, Y., Han, M., Li, H., Tao, Z., Niu, Z., and Chen, J. (2018). Nafion/Titanium Dioxide-Coated Lithium Anode for Stable Lithium-Sulfur Batteries. Chem. Asian J. *13*, 1379–1385.

45. Xu, R., Zhang, X.-Q., Cheng, X.-B., Peng, H.-J., Zhao, C.-Z., Yan, C., and Huang, J.-Q. (2018). Artificial Soft-Rigid Protective Layer for Dendrite-Free Lithium Metal Anode. Adv. Funct. Mater. *28*, 1705838.

46. Kim, J.-H., Woo, H.-S., Kim, W.K., Ryu, K.H., and Kim, D.-W. (2016). Improved Cycling Performance of Lithium-Oxygen Cells by Use of a Lithium Electrode Protected with Conductive Polymer and Aluminum Fluoride. ACS Appl. Mater. Interfaces *8*, 32300–32306.

47. Kwak, W.-J., Park, S.-J., Jung, H.-G., and Sun, Y.-K. (2018). Optimized Concentration of Redox Mediator and Surface Protection of Li Metal for Maintenance of High Energy Efficiency in Li-O_2 Batteries. Adv. Energy Mater. *8*, 1702258.

48. Liu, K., Pei, A., Lee, H.R., Kong, B., Liu, N., Lin, D., Liu, Y., Liu, C., Hsu, P.C., Bao, Z., and Cui, Y. (2017). Lithium Metal Anodes with an Adaptive "Solid-Liquid" Interfacial Protective Layer. J. Am. Chem. Soc. *139*, 4815–4820.

49. Zheng, G., Wang, C., Pei, A., Lopez, J., Shi, F., Chen, Z., Sendek, A.D., Lee, H.-W., Lu, Z., Schneider, H., et al. (2016). High-Performance Lithium Metal Negative Electrode with a Soft and Flowable Polymer Coating. ACS Energy Lett. *1*, 1247–1255.

50. Cao, P.-F., Li, B., Hong, T., Xing, K., Voylov, D.N., Cheng, S., Yin, P., Kisliuk, A., Mahurin, S.M., Sokolov, A.P., and Saito, T. (2017). Robust and Elastic Polymer Membranes with Tunable Properties for Gas Separation. ACS Appl. Mater. Interfaces *9*, 26483–26491.

51. Cao, P.-F., Li, B., Hong, T., Townsend, J., Qiang, Z., Xing, K., Vogiatzis, K.D., Wang, Y., Mays, J.W., Sokolov, A.P., et al. (2018). Superstretchable, Self-Healing Polymeric Elastomers with Tunable Properties. Adv. Funct. Mater. *28*, 1800741.

52. Cao, P.-F., Li, B., Yang, G., Zhao, S., Townsend, J., Xing, K., Qiang, Z., Vogiatzis, K.D., Sokolov, A.P., Nanda, J., et al. (2020). Elastic Single-Ion Conducting Polymer Electrolytes: Toward a Versatile Approach for Intrinsically Stretchable Functional Polymers. Macromolecules *53*, 3591–3601.

53. Fan, L., Zhuang, H.L., Zhang, W., Fu, Y., Liao, Z., and Lu, Y. (2018). Stable Lithium Electrodeposition at Ultra-High Current Densities Enabled by 3D PMF/Li Composite Anode. Adv. Energy Mater. *8*, 1703360.

54. Liu, W., Mi, Y., Weng, Z., Zhong, Y., Wu, Z., and Wang, H. (2017). Functional metal-organic framework boosting lithium metal anode

performance *via* chemical interactions. Chem. Sci. (Camb.) *8*, 4285–4291.

55. Kim, D., Liu, X., Yu, B., Mateti, S., O'Dell, L.A., Rong, Q., and Chen, Y. (2020). Amine-Functionalized Boron Nitride Nanosheets: A New Functional Additive for Robust, Flexible Ion Gel Electrolyte with High Lithium-Ion Transference Number. Adv. Funct. Mater. *30*, 1910813.

56. Pan, Y., Ge, S., Rashid, Z., Gao, S., Erwin, A., Tsukruk, V., Vogiatzis, K.D., Sokolov, A.P., Yang, H., and Cao, P.-F. (2020). Adhesive Polymers as Efficient Binders for High-Capacity Silicon Electrodes. ACS Appl. Energy Mater. *3*, 3387–3396.

57. Zhang, Y., Lv, W., Huang, Z., Zhou, G., Deng, Y., Zhang, J., Zhang, C., Hao, B., Qi, Q., He, Y.-B., et al. (2019). An Air-Stable and Waterproof Lithium Metal Anode Enabled by Wax Composite Packaging. Sci. Bull. (Beijing) *64*, 910–917.

58. Zhang, C., Lan, Q., Liu, Y., Wu, J., Shao, H., Zhan, H., and Yang, Y. (2019). A Dual-Layered Artificial Solid Electrolyte Interphase Formed by Controlled Electrochemical Reduction of LiTFSI/DME-LiNO$_3$ for Dendrite-Free Lithium Metal Anode. Electrochim. Acta *306*, 407–419.

59. Xiao, J., Li, Q., Bi, Y., Cai, M., Dunn, B., Glossmann, T., Liu, J., Osaka, T., Sugiura, R., Wu, B., et al. (2020). Understanding and Applying Coulombic Efficiency in Lithium Metal Batteries. Nat. Energy *5*, 561–568.

60. Li, Q., Zeng, F.-L., Guan, Y.-P., Jin, Z.-Q., Huang, Y.-Q., Yao, M., Wang, W.-K., and Wang, A.-B. (2018). Poly (dimethylsiloxane) Modified Lithium Anode for Enhanced Performance of Lithium-Sulfur Batteries. Energy Storage Mater. *13*, 151–159.

61. Chi, S.-S., Liu, Y., Song, W.-L., Fan, L.-Z., and Zhang, Q. (2017). Prestoring Lithium into Stable 3D Nickel Foam Host as Dendrite-Free Lithium Metal Anode. Adv. Funct. Mater. *27*, 1700348.

62. Liu, W., Lin, D., Pei, A., and Cui, Y. (2016). Stabilizing Lithium Metal Anodes by Uniform Li-Ion Flux Distribution in Nanochannel Confinement. J. Am. Chem. Soc. *138*, 15443–15450.

63. Yang, C., Liu, B., Jiang, F., Zhang, Y., Xie, H., Hitz, E., and Hu, L. (2017). Garnet/Polymer Hybrid Ion-Conducting Protective Layer for Stable Lithium Metal Anode. Nano Res. *10*, 4256–4265.

64. Zhao, S., Zhang, Y., Pham, H., Carrillo, J.-M.Y., Sumpter, B.G., Nanda, J., Dudney, N.J., Saito, T., Sokolov, A.P., and Cao, P.-F. (2020). Improved Single-Ion Conductivity of Polymer Electrolyte via Accelerated Segmental Dynamics. ACS Appl. Energy Mater. *3*, 12540–12548.

65. Luo, J., Fang, C.-C., and Wu, N.-L. (2018). High Polarity Poly(vinylidene difluoride) Thin Coating for Dendrite-Free and High-Performance Lithium Metal Anodes. Adv. Energy Mater. *8*, 1701482.

66. Chen, S., Niu, C., Lee, H., Li, Q., Yu, L., Xu, W., Zhang, J.-G., Dufek, E.J., Whittingham, M.S., Meng, S., et al. (2019). Critical Parameters for Evaluating Coin Cells and Pouch Cells of Rechargeable Li-Metal Batteries. Joule *3*, 1094–1105.

67. Qi, L., Shang, L., Wu, K., Qu, L., Pei, H., Li, W., Zhang, L., Wu, Z., Zhou, H., McKeown, N.B., et al. (2019). An Interfacial Layer Based on Polymers of Intrinsic Microporosity to Suppress Dendrite Growth on Li Metal Anodes. Chemistry *25*, 12052–12057.

68. Xu, B., Zhai, H., Liao, X., Qie, B., Mandal, J., Gong, T., Tan, L., Yang, X., Sun, K., Cheng, Q., et al. (2019). Porous Insulating Matrix for Lithium Metal Anode with Long Cycling Stability and High Power. Energy Storage Mater. *17*, 31–37.

69. Li, N.-W., Shi, Y., Yin, Y.-X., Zeng, X.-X., Li, J.-Y., Li, C.-J., Wan, L.-J., Wen, R., and Guo, Y.-G. (2018). A Flexible Solid Electrolyte Interphase Layer for Long-Life Lithium Metal Anodes. Angew. Chem. Int. Ed. Engl. *57*, 1505–1509.

70. Li, S., Fan, L., and Lu, Y. (2019). Rational Design of Robust-Flexible Protective Layer for Safe Lithium Metal Battery. Energy Storage Mater. *18*, 205–212.

71. Gao, S., Sun, F., Liu, N., Yang, H., and Cao, P.-F. (2020). Ionic Conductive Polymers as Artificial Solid Electrolyte Interphase Films in Li Metal Batteries–A Review. Mater. Today *40*, 140–159.

72. Yu, Z., Mackanic, D.G., Michaels, W., Lee, M., Pei, A., Feng, D., Zhang, Q., Tsao, Y., Amanchukwu, C.V., Yan, X., et al. (2019). A Dynamic, Electrolyte-Blocking, and Single-Ion-Conductive Network for Stable Lithium-Metal Anodes. Joule *3*, 2761–2776.

73. Li, N., Wei, W., Xie, K., Tan, J., Zhang, L., Luo, X., Yuan, K., Song, Q., Li, H., Shen, C., et al. (2018). Suppressing Dendritic Lithium Formation Using Porous Media in Lithium Metal-Based Batteries. Nano Lett. *18*, 2067–2073.

74. Liu, Y., Lin, D., Yuen, P.Y., Liu, K., Xie, J., Dauskardt, R.H., and Cui, Y. (2017). An Artificial Solid Electrolyte Interphase with High Li-Ion Conductivity, Mechanical Strength, and Flexibility for Stable Lithium Metal Anodes. Adv. Mater. *29*, 1605531.

75. Plimpton, S., and Hendrickson, B. (1996). A New Parallel Method for Molecular Dynamics Simulation of Macromolecular Systems. J. Comput. Chem. *17*, 326–337.

76. Tan, J., and Ryan, E.M. (2016). Structured Electrolytes to Suppress Dendrite Growth in High Energy Density Batteries. Int. J. Energy Res. *40*, 1800–1810.

77. Tan, J., Cannon, A., and Ryan, E. (2020). Simulating Dendrite Growth in Lithium Batteries under Cycling Conditions. J. Power Sources *463*, 228187.

78. Wei, W., Ihrfors, C., Björefors, F., and Nyholm, L. (2020). Capacity Limiting Effects for Freestanding, Monolithic TiO$_2$ Nanotube Electrodes with High Mass Loadings. ACS Appl. Energy Mater. *3*, 4638–4649.

79. Luo, J., Lee, R.-C., Jin, J.-T., Weng, Y.-T., Fang, C.-C., and Wu, N.-L. (2017). A dual-functional polymer coating on a lithium anode for suppressing dendrite growth and polysulfide shuttling in Li-S batteries. Chem. Commun. (Camb.) *53*, 963–966.

80. Tan, J., Tartakovsky, A.M., Ferris, K., and Ryan, E.M. (2015). Investigating the Effects of Anisotropic Mass Transport on Dendrite Growth in High Energy Density Lithium Batteries. J. Electrochem. Soc. *163*, A318–A327.

81. Elezgaray, J., Lége, C., and Argoul, F. (1998). Linear Stability Analysis of Unsteady Galvanostatic Electrodeposition in the Two-Dimensional Diffusion-Limited Regime. J. Electrochem. Soc. *145*, 2016–2024.